Near Invariance of Poleward Atmospheric Heat Transport in Response to Midlatitude Orography

TYLER COX,[a] AARON DONOHOE,[b] GERARD H. ROE,[c] KYLE C. ARMOUR,[a,d] AND DARGAN M. W. FRIERSON[a]

[a] *Department of Atmospheric Sciences, University of Washington, Seattle, Washington*
[b] *Polar Science Center/Applied Physics Lab, University of Washington, Seattle, Washington*
[c] *Department of Earth and Space Sciences, University of Washington, Seattle, Washington*
[d] *School of Oceanography, University of Washington, Seattle, Washington*

(Manuscript received 12 November 2021, in final form 22 February 2022)

ABSTRACT: Total poleward atmospheric heat transport (AHT) is similar in both magnitude and latitudinal structure between the Northern and Southern Hemispheres. These similarities occur despite more major mountain ranges in the Northern Hemisphere, which help create substantial stationary eddy AHT that is largely absent in the Southern Hemisphere. However, this hemispheric difference in stationary eddy AHT is compensated by hemispheric differences in other dynamic components of AHT so that total AHT is similar between hemispheres. To understand how AHT compensation occurs, we add midlatitude mountain ranges in two different general circulation models that are otherwise configured as aquaplanets. Even when midlatitude mountains are introduced, total AHT is nearly invariant. We explore the near invariance of total AHT in response to orography through dynamic, energetic, and diffusive perspectives. Dynamically, orographically induced changes to stationary eddy AHT are compensated by changes in both transient eddy and mean meridional circulation AHT. This creates an AHT system with three interconnected components that resist large changes to total AHT. Energetically, the total AHT can only change if the top-of-the-atmosphere net radiation changes at the equator-to-pole scale. Midlatitude orography does not create large-enough changes in the equator-to-pole temperature gradient to alter outgoing longwave radiation enough to substantially change total AHT. In the zonal mean, changes to absorbed shortwave radiation also often compensate for changes in outgoing longwave radiation. Diffusively, the atmosphere smooths anomalies in temperature and humidity created by the addition of midlatitude orography, such that total AHT is relatively invariant.

SIGNIFICANCE STATEMENT: The purpose of this study is to better understand how orography influences heat transport in the atmosphere. Enhancing our understanding of how atmospheric heat transport works is important, as heat transport helps moderate Earth's surface temperatures and influences precipitation patterns. We find that the total amount of atmospheric heat transport does not change in the presence of mountains in the midlatitudes. Different pieces of the heat transport change, but they change in compensatory ways, such that the total heat transport remains roughly constant.

KEYWORDS: Atmospheric circulation; Eddies; Fluxes; Stationary waves; Heat budgets/fluxes

1. Introduction

Poleward atmospheric heat transport (AHT) is a critical element of the climate system, moderating the equator-to-pole temperature gradient and carrying the water vapor of the hydrologic cycle (e.g., Pierrehumbert 2010; Held and Soden 2006; Siler et al. 2018). The observed annual-mean total AHT is similar between hemispheres (Figs. 1a,e), despite there being more land and more substantial mountain ranges in the Northern Hemisphere. The distribution of mountains and land create stationary Rossby waves, which enhance zonal asymmetries in temperature and precipitation and contribute to AHT (e.g., Manabe and Terpstra 1974; Hoskins and Karoly 1981; Broccoli and Manabe 1992; Held et al. 2002).

It is useful to deconstruct AHT into three dynamical components (e.g., Holton and Hakim 2013). We deconstruct and define AHT as

$$\mathrm{AHT}(\phi) = \frac{2\pi a\cos(\phi)}{g}\int_0^{P_s} \underbrace{[\overline{V}][\overline{\mathrm{MSE}}]}_{\mathrm{MMC}} + \underbrace{[\overline{V}^{*}\,\overline{\mathrm{MSE}}^{*}]}_{\mathrm{SE}} + \underbrace{[\overline{V^{*\prime}\,\mathrm{MSE}^{*\prime}}] + \overline{[V]'[\mathrm{MSE}]'}}_{\mathrm{TE}}\,dp, \tag{1}$$

where the integral is over pressure p from the top-of-atmosphere (TOA) to the surface, square brackets [] denote zonal averages, overbars $\overline{()}$ denote time averages, asterisks (*) are departures from the zonal average, and primes (′) are departures from the time average. The term ϕ is latitude, V is the meridional velocity, and MSE is the moist static energy, defined as

$$\mathrm{MSE} = c_p T + L_v q + gZ, \tag{2}$$

where c_p is the specific heat of air, T is the atmospheric temperature, L_v is the latent heat of vaporization of water, q is the specific humidity, g is the acceleration of gravity, and Z is the geopotential height.

The first term in Eq. (1) is the component due to the mean meridional circulation (MMC), which is calculated from the

---

Corresponding author: Tyler Cox, tylersc@uw.edu

DOI: 10.1175/JCLI-D-21-0888.1

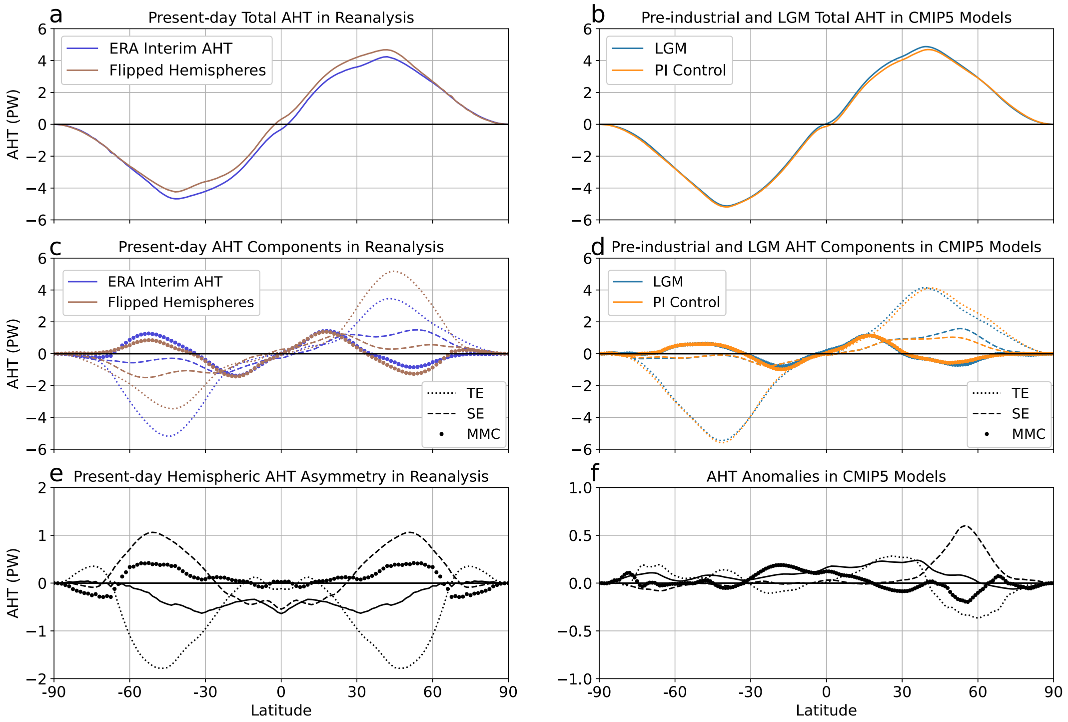

FIG. 1. (a) Total AHT and (c) the dynamic AHT components for the climatological AHT from ERA-Interim (light purple) and the same values flipped across the equator (brown); (b) total AHT and (d) the dynamic AHT components for the climatological AHT from CMIP5 ensemble means for preindustrial (black) and Last Glacial Maximum (blue) conditions; (e) the anomalies, Southern Hemisphere minus Northern Hemisphere, in AHT between hemispheres from ERA-Interim; and (f) the anomalies, LGM minus PI control, in AHT between preindustrial and the LGM from the CMIP5 ensemble (calculations from Donohoe et al. 2020).

time-mean and zonal-mean fields. We account for conservation of mass by removing the vertically averaged MSE (Marshall et al. 2014; Donohoe et al. 2020). The second term is the stationary eddy (SE) component, which is calculated from the time-mean zonal anomalies. The third and fourth terms are collectively called the transient eddy (TE) component, although we note that the fourth term is much smaller than the third (Marshall et al. 2014).

The contrasting land and mountain distributions between Northern and Southern Hemispheres give rise to differences in these dynamic components. Specifically, the AHT carried by SEs is much larger in the midlatitudes of the Northern Hemisphere than at equivalent latitudes of the Southern Hemisphere (Figs. 1c,e). The difference in poleward AHT by SEs between the Northern Hemisphere and Southern Hemisphere at each latitude peaks at 1.1 PW (Fig. 1e). In contrast, the hemispheric difference in total AHT (solid lines, Figs. 1a,e) is relatively smaller, peaking at only 0.6 PW. That is, the hemispheric asymmetry in SE AHT is compensated by hemispheric asymmetries in the AHT associated with the MMC and TEs. Moreover, the total AHT varies smoothly with latitude with a shape that is similar between hemispheres, despite both the strong latitudinal structure and the hemispheric asymmetries of the individual dynamic components (Trenberth and Stepaniak 2003). For these reasons, we refer to total AHT as relatively invariant between the Northern and Southern Hemispheres. We note the hemispheric asymmetry of total heat transport by the ocean and atmosphere combined is smaller than that in AHT alone (Donohoe et al. 2020), but we will focus exclusively on AHT in this manuscript.

Perhaps even more striking is that both the hemispheric symmetry and the smoothness of total AHT seen in the modern climate persist in general circulation model (GCM) simulations of the Last Glacial Maximum (LGM). Although large Northern Hemisphere ice sheets disrupt the circulation patterns in the mid- to high latitudes of the Northern Hemisphere, creating additional SE AHT (e.g., Cook and Held 1988; Donohoe et al. 2020), total AHT remains relatively invariant (Figs. 1b,f) due to compensating decreases in TE AHT (Li and Battisti 2008). These examples motivate the primary question this work addresses: how is total AHT so nearly invariant and smoothly varying with latitude in response to midlatitude orography even while SE AHT changes so substantially? Although land distribution, ocean heat transport, and orography impact AHT, this work will focus on the effect of orography.

Previous research has characterized AHT through three different perspectives (e.g., Armour et al. 2019). The first perspective characterizes AHT through the atmosphere's dynamic motions, as defined in Eq. (1). Total AHT is dominated by the MMC and SEs in the tropics and then gradually becomes dominated by eddies poleward of 25° latitude (Fig. 1c). This perspective on AHT will be referred to as the *dynamic* perspective. Although the dynamic perspective is necessary in order to characterize how atmospheric circulations supply the observed AHT, it has not traditionally offered an obvious way to understand why total AHT is invariant and smoothly varying with latitude (e.g., Armour et al. 2019).

A second perspective is that AHT can be characterized through the energetic requirements implied by the TOA radiation and surface energy budgets. The imbalance between incoming and outgoing radiation must be balanced by meridional heat transport within the Earth system (e.g., Stone 1978). This meridional transport can be accomplished by both the atmosphere and the ocean, but we focus on the atmospheric part in this work, in part because it dominates outside of the deep tropics (e.g., Farneti and Vallis 2013). From this perspective, the smoothness of AHT with latitude is mandated by the smoothness of net TOA radiation (Trenberth and Stepaniak 2003). Moreover, AHT changes must be accompanied by changes in net TOA radiation (absent changes in ocean heat transport). However, due to the coupling between radiation and circulation, it can be difficult to determine which, if either, is more fundamental in driving AHT changes (Cox et al. 2021). We refer to this perspective on AHT as the *energetic* perspective.

A third perspective on AHT comes from Earth's tendency to move energy downgradient. Previous work has shown that a general principle of downgradient diffusion of near-surface MSE accurately captures AHT and its changes (Flannery 1984; Hwang et al. 2011; Roe et al. 2015; Bonan et al. 2018; Merlis and Henry 2018; Siler et al. 2018; Armour et al. 2019). From this perspective, AHT is smoothly varying because the MSE gradient varies smoothly with latitude. Theory suggests that TEs in the midlatitudes efficiently mix MSE (Held 1999), supporting the idea that a diffusive perspective may work in the midlatitudes. Recent research has shown downgradient transport works surprisingly well at all latitudes, even those not dominated by TE AHT (Armour et al. 2019). This downgradient diffusion principle is referred to as the *diffusive* perspective.

Previous work about AHT invariance involves compensation between the atmospheric circulations that contribute to AHT. This work does not try to present a comprehensive summary of all mechanisms responsible for AHT invariance, but highlights those we find most important in our work. From the dynamic perspective, orography induces a stationary atmospheric circulation with associated SE AHT anomalies (e.g., Manabe and Terpstra 1974; Broccoli and Manabe 1992; Held et al. 2002). These changes in SE AHT are often accompanied by opposite-signed changes in TE AHT, such that total AHT changes by a smaller magnitude than the SE AHT changes alone (Manabe and Terpstra 1974; Kaspi and Schneider 2013). This SE and TE compensation principle has theoretical justification, as SEs can modify the baroclinicity that TEs rely on while TEs and the heating associated with them can help drive SEs (e.g., Branstator 1995; Chang et al. 2002; Held et al. 2002; Inatsu et al. 2003; Kaspi and Schneider 2013), and has been found to be important in current and past climates (Donohoe et al. 2020). Additional dynamic connections exist between eddy AHT convergence and Ferrel cell AHT (e.g., Sasamori 1978; Salustri and Stone 1983), and eddy momentum fluxes and Hadley cell strength (e.g., Walker and Schneider 2006).

From the energetic perspective, AHT will remain relatively invariant if orography does not induce substantial changes in TOA or surface energy fluxes. However, orography can change both shortwave and longwave radiation fluxes through its effects on cloud cover and temperature patterns. Kiehl (1994) found that compensation often occurs between cloud shortwave and longwave radiation effects in the tropics. In general, cloud longwave and shortwave effects do not cancel out. This is indicated by the substantial intermodel spread of mean state cloud radiative effects, which lead to intermodel differences in AHT of order 20% (Donohoe and Battisti 2012).

From the diffusive perspective, anomalies created by the addition of orography will be smoothed through downgradient energy transport. Specifically, the anomalous SE AHT associated with orography will (in the absence of other changes) reduce the equator-to-pole MSE gradient thereby reducing the diffusive AHT by TEs. The extent to which these SE AHT anomalies are smoothed, and the extent to which total AHT remains invariant, are dependent on the size of the anomalies and the diffusivity of the atmosphere.

This work explores the ways in which AHT compensation occurs, from each of these three AHT perspectives, and the extent to which total AHT can remain invariant with the addition of midlatitude orography. To do so, we study the AHT response to the addition of idealized mountain ridges to the midlatitudes of each hemisphere in two aquaplanet atmospheric GCMs. This idealized modeling setup (explained in more detail in section 2) allows us to study the mechanisms of AHT changes without the full complexity found in comprehensive GCMs or nature. We then test the sensitivity of our results, and reintroduce some complexity, by adding a seasonal cycle.

2. Model setup

One mechanism that might contribute to AHT invariance is compensation between changes in absorbed shortwave radiation (ASR) and outgoing longwave radiation (OLR). Therefore we use two models of different radiative complexity. The first model is a gray radiation model with no clouds or water vapor feedbacks; temperature anomalies are radiatively damped only by the Planck response. The specific model we use is GRaM from Frierson et al. (2006) adapted to use the convection scheme from Frierson (2007). Shortwave radiation is not absorbed in the atmosphere, and longwave radiation is absorbed and emitted per a prescribed optical depth. The insolation in GRaM is adjusted to mimic the effect of clouds and surface albedo in order to give a more realistic value for total AHT (see Frierson et al. (2006) for full details). The second model we use is the Geophysical Fluid Dynamics

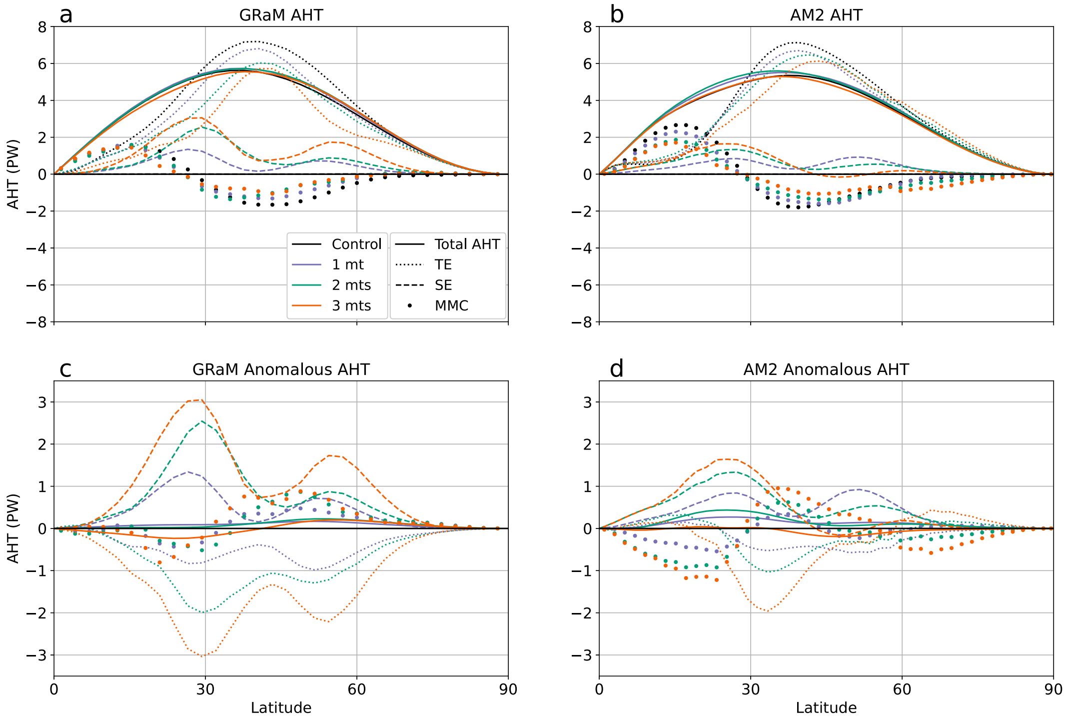

FIG. 2. Total AHT and its dynamic components for (a) GRaM and (b) AM2 and the anomalous AHT for (c) GRaM and (d) AM2, where anomalies are calculated as mountain simulation minus control. Different colors denote ridge cases, and different line styles show the different dynamical components for each case. Results shown are the mean of the Northern and Southern Hemispheres (with the Southern Hemisphere sign flipped), which are symmetric by design.

Laboratory's AM2 (Anderson et al. 2004), which has a more complex radiation scheme including atmospheric shortwave absorption, and cloud and water-vapor feedbacks. Both models are initially run as aquaplanets at perpetual equinox conditions with no land or sea ice and a shallow mixed layer depth of 2.4 m to enable rapid model spin up. AM2 simulations are run for 20 years, with the last 18 years used for analysis, while GRaM simulations are run for 10 years, with the last 8 used for analysis. The shorter simulation time in GRaM is sufficient to capture an accurate climatology due to its simpler radiation scheme than AM2. Climatological AHT is realistic in both models (Figs. 2a,b), but is higher than observations due to the absence of ocean heat transport.

Using these two models, we test the impact of large-scale mountain ranges (referred to here as ridges), similar in style to those used by Wills and Schneider (2016). These lozenge-shaped ridges are described by the following formula:

$$z(\lambda, \phi) = h_0 \exp\left[\frac{(\lambda - \lambda_0)^2}{2{\sigma_\lambda}^2} - \frac{\max(0, |\phi - \phi_0| - R)^2}{2{\sigma_\phi}^2}\right], \qquad (3)$$

where λ is the longitude in degrees, ϕ is the latitude in degrees, $h_0 = 4000$ m, $\phi_0 = 40°$, $R = 4°$, $\sigma_\lambda = 12.5°$, and $\sigma_\phi = 8°$. When more than one ridge is included, λ_0 is chosen such that the ridges are equally spaced in each hemisphere. Meridional cross sections of these ridges are plateaus, with flat sections of meridional extent $2R$, bounded by Gaussian-shaped slopes, while longitudinal cross sections are Gaussian in shape. The surface type remains a mixed-layer slab of water throughout, so these mountains can be described as "water ridges."

The size, shape, and location of orographic features all affect the SE response, and therefore may affect the degree of AHT compensation. We perform simulations with one, two, or three mountain ridges in each of the Northern and Southern Hemispheres (mirrored symmetrically across the equator) located between 20° and 60°. Different numbers of mountain ridges generally create different magnitudes of SE AHT (dashed lines, Figs. 2c,d). Therefore, by adding in one, two, or three mountain ridges we can test how the magnitude of disruption affects the ability of the atmosphere to maintain nearly invariant total AHT. We also tested a variety of other orographic configurations including ridges of different heights and at different latitudes (not shown), as previous work has suggested that tropically forced stationary waves may lead to changes in total AHT (Baggett and Lee 2017; Park and Lee 2019). We found that the specific mountain configuration, even the addition of tropical mountains, did not substantially affect our main findings regarding the near invariance of AHT in response to orography.

3. Results

Figure 2 summarizes the main results of our simulations from GRaM (left-hand panels) and AM2 (right-hand panels). The total AHT and its dynamic components are shown for

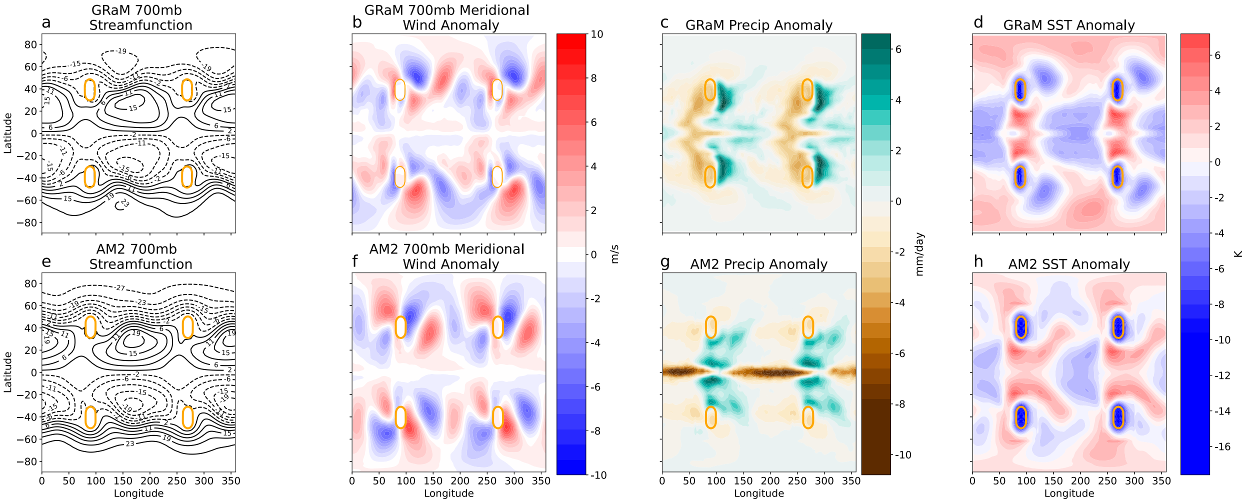

FIG. 3. (top) Results from GRaM and (bottom) results from AM2. (a),(e) 700-hPa streamfunctions (contours are in units of 10^6 m^2 s^{-1}); (b),(f) 700-hPa meridional wind anomalies; (c),(g) precipitation anomalies; and (d),(h) sea surface temperature anomalies. Anomalies are calculated as two-mountain simulation minus control. Orange contours are the 700-hPa surface pressure contours to show the general position of the mountains.

the control (no ridges), and for the one-, two-, and three-ridge cases in the top panels. The anomalies from the control case are shown in the lower panels. Results are presented for only one hemisphere, as the hemispheres are symmetric by design. For all experiments, the addition of orography introduces substantial SE AHT (dashed lines), but there is a larger impact in GRaM than in AM2. For the three-ridge case in GRAM, SEs contribute a maximum of about 3 PW to total AHT (Fig. 2c) near 30° latitude.

Despite the large SE AHT induced by the orography, total AHT remains nearly invariant in both GRaM and AM2 (solid lines in Figs. 2c,d). Total AHT changes never exceed 0.5 PW, and are under 0.25 PW at most latitudes. That is, substantial changes in individual AHT dynamic components are compensated such that total AHT changes by less than any of the individual dynamic components. This compensation between AHT dynamic components is further explored in section 3a. The changes in total AHT are smaller in GRaM than in AM2, suggesting compensation is better in GRaM. In both models, compensation of SE AHT changes occurs through changes in both TE and MMC AHT, with the relative importance of each depending on latitude and model.

Total AHT changes are smaller in our simulations compared to previous work that introduced SEs intro GCMs. Manabe and Terpstra (1974) split the total AHT into dry and moist components. They found little change in the poleward moist AHT and relatively large changes in poleward dry AHT after the introduction of orography, while this work finds little change in both dry and moist AHT in the midlatitudes (not shown). This may be due in part to the fixed surface temperatures used in Manabe and Terpstra (1974). Using a modeling setup similar to GRaM, Kaspi and Schneider (2013) also found larger changes in total AHT when they induced SEs through the use of zonal anomalies in surface heating. This suggests that the degree of AHT compensation may be influenced by the method of inducing SEs.

We first characterize the effects that the mountains have on atmospheric circulations, and then evaluate how the AHT compensation occurs through the dynamic, energetic, and diffusive perspectives. To reduce the results presented to a manageable amount, we will focus on the two-ridge case. The main aspects of the circulation response do not depend on the number of ridges, although in the three-ridge case there is some interference between the responses to individual ridges. We will describe the circulation changes from a Northern Hemisphere perspective (although the hemispheres are symmetric).

In general, the circulation response of the atmosphere is similar to that seen in other modeling simulations that introduce idealized orography (e.g., Manabe and Terpstra 1974; Broccoli and Manabe 1992; Held et al. 2002). We focus here on elements of the atmospheric response that are most relevant to AHT or differ from previous work.

The circulation of the lower troposphere is strongly disrupted by the addition of the orography as is seen in the climatological streamfunctions at 700 hPa in Figs. 3a and 3e [streamfunctions calculated using the "windspharm" Python package, Dawson (2016)]. The main circulation response can be characterized as flow splitting ahead of the orography: streamlines impinging on the southwestern side of the ridges bow southward, and streamlines impinging on the northwestern side bow poleward. The flow splitting upwind of the ridges is also evident in the quadrupole structure of the meridional wind anomalies (Figs. 3b,f). Flow can also be deflected over the top of the mountains, but the ridges' size and latitudinal position make flow splitting more favorable (e.g., Trenberth and Chen 1988; Ringler and Cook 1997; Rodwell and Hoskins 1996). In fact, the low-level westerly flow impinging on the southwest portion of the mountains is so strongly deflected that it turns back to join the easterly trade winds (Figs. 3a,e). This is likely because the equatorward-dipping isentropes make it particularly hard for the flow to move over the southern end of the mountains (e.g., Valdes and Hoskins 1991;

Takahashi and Battisti 2007a; Brayshaw et al. 2009), and so helps build the anticyclonic flow that is evident in the streamfunctions between the ridges in subtropical latitudes. To the lee of each ridge there is convergence where the flow enters the region of locally enhanced streamfunction gradients (Figs. 3a,e). This results in a storm track that begins in the lee of the topography and tracks into the northeastward-tilting region of stronger flow, although the specific patterns and amplitudes differ between the models. This storm-track response has been seen in previous work (e.g., Hoskins and Valdes 1990; Brayshaw et al. 2009; Cash et al. 2005; Inatsu et al. 2002), and is reminiscent of the Atlantic and Pacific storm tracks in the lee of the Rockies and Tibetan Plateau, respectively.

The flow splitting ahead of the orography induces anomalous meridional winds, which generally bring associated anomalies in temperature via advection of the mean-state meridional temperature gradients. In regions of anomalous southerly flow on the northwest and southeast sides of the mountains, warm-air advection causes positive temperature anomalies, while in regions of anomalous northerly flow on the northeast and southwest sides of the mountains, cold-air advection causes negative temperature anomalies (Figs. 3d,h). Cloud changes in AM2 also modify the magnitude of the temperature anomalies, particularly to the northeast of each mountain. The combination of wind anomalies (Figs. 3b,f) and temperature anomalies (Figs. 3d,h) gives rise to anomalous SE AHT, which will be further explored in section 3a.

The orography creates some dramatic impacts on the precipitation patterns (Figs. 3c,g). Strikingly, neither model displays the classic west–east orographic rain shadow that might be expected for westerly impinging flow. Instead, there is drying to the west, and particularly the southwest, of the mountains. This drying is due to subsidence from both the divergence of the zonal wind, as the flow is divided into northern and southern routes around the mountains, and the equatorward velocity anomaly (Figs. 3b,f), which is balanced by subsidence to maintain Sverdrup balance (Rodwell and Hoskins 2001; Takahashi and Battisti 2007b). This drying is also seen, albeit to a weaker and smaller spatial extent, in Brayshaw et al. (2009). Enhanced precipitation occurs on the eastern side of the mountains where the diverted flow converges and poleward velocity anomalies induce rising motion. Maps of anomalous vertical velocity (not shown) appear similar to those of precipitation. There is no substantial upward vertical velocity on the western side of the mountains suggesting that most of the flow is deflected around the mountains rather than over them. A more typical, albeit weak, west–east orographic rain shadow does occur in our simulations with smaller ($h_0 = 2500$ m) ridges where westerly flow is more able to move over rather than around the ridges (not shown).

a. Dynamic perspective on AHT response to orography

In this section we evaluate the impact of the orography on AHT from a dynamical perspective. There are large changes in the individual dynamic components of AHT (Figs. 2c,d): up to 3 PW in GRaM and 2 PW in AM2 even though, as already noted, changes in total AHT are less than 0.25 PW at most latitudes. How do the individual dynamical components adjust to achieve this overall near invariance of total AHT?

In most of our simulations, the AHT associated with the SEs induced by the orography forms a two-peaked structure with peaks at approximately 25° and 55°, and a local minimum near the center of the prescribed orography at 40°. The equatorward peak in SE AHT is generally larger than the poleward peak, although the magnitude of each peak is dependent on the model and number of ridges (dashed lines in Figs. 2c,d). In GRaM, SE AHT increases with the number of ridges for both the 25° and 55° peaks, albeit nonlinearly; while in AM2, SE AHT increases at the peak at 25° but decreases for the peak at 55°, which nearly disappears for the three-ridge case. This decrease in AM2 is due to weaker fluxes of temperature and moisture around the northern side of each ridge (not shown).

The adjustment of the other two dynamic components of AHT to the introduction of orography differs between the two models. The TE AHT decreases at most latitudes in both models (dotted lines in Figs. 2c,d). However, in GRaM the pattern of TE AHT decrease closely matches the double peaked pattern of SE AHT increases, but with the opposite sign; whereas in AM2 the pattern of TE AHT decrease has one peak at about 35° latitude. The patterns of the changes in MMC AHT are similar in both models (dots in Figs. 2c,d), although the magnitude of the changes is larger in AM2. There is a decrease in MMC AHT in the subtropics and an increase in midlatitudes; and a negative anomaly of MMC AHT in the high latitudes in AM2, but not in GRaM. Overall, from Fig. 2 we see that, in GRaM, the primary compensation occurs between the SE and TE transports; while in AM2 it is a three-way balance, with compensation from the MMC being particularly important in the subtropics.

Changes to individual dynamic components of AHT do not happen in isolation from one another. As mentioned previously, there are established mechanisms for how the dynamic components interact, and those mechanisms tend to produce compensation. Kaspi and Schneider (2013) show how SEs modify the baroclinicity by altering moist-static energy gradients. At latitudes where ridges drive SE AHT, the zonal-mean MSE gradient is decreased, reducing the TE AHT that relies on these gradients. Moreover, the Ferrel cell is partially driven by changes in the convergence of AHT by both SEs and TEs (e.g., Sasamori 1978; Salustri and Stone 1983) such that increases to eddy AHT convergence will strengthen the Ferrel cell. The climatological Ferrel cell AHT is equatorward, so a strengthened Ferrel cell transports more heat equatorward, compensating for the increased AHT convergence by the eddies. Decreased eddy AHT convergence has the opposite effect, resulting in a weakened Ferrel cell, and less equatorward AHT to compensate for decreased AHT convergence by the eddies. A final major connection between dynamic components is the influence that eddy momentum fluxes have on Hadley cell strength (e.g., Walker and Schneider 2006). Increases in eddy momentum flux divergence in the Hadley cell region strengthen the Hadley cell, while the opposite is also true. In this way, changes to extratropical circulation can influence tropical circulation patterns. A hallmark of all these

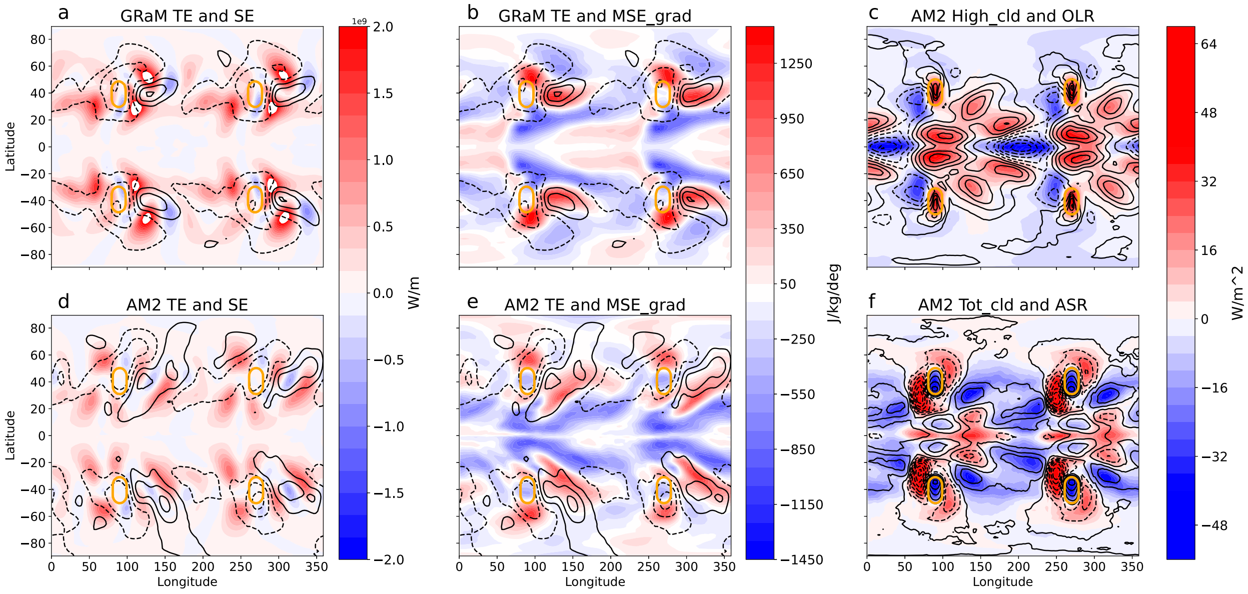

FIG. 4. The two leftmost columns compare results from (top) GRaM and (bottom) AM2. (a),(d) Anomalies in local SE AHT (colors) and local TE AHT (black contours; interval = 9×10^8 W m^{-1}); and (b),(e) anomalies in near-surface MSE gradient (colors) and local TE AHT (black contours; interval = 9×10^8 W m^{-1}). The rightmost column shows cloud and radiation output fields from AM2. (c) Anomalies in OLR (colors) and high-cloud fraction (black contours, interval = 0.018); and finally, (f) anomalies in ASR (colors) and total cloud fraction (black contours, interval = 0.018). Anomalies are calculated as two-mountain simulation minus control. AHT is defined as positive poleward in both hemispheres and the climatological MSE gradient is defined as positive in both hemispheres. Orange contours are the 700-hPa surface pressure contours to show the general position of the mountains.

mechanisms is that they tend to be compensatory: a change in one dynamic component is typically mitigated by an opposite-signed change in another dynamic component. Together, they create an interacting system of dynamic components that, in aggregate, resist changes in total AHT.

We can better understand some features of the dynamic AHT components in our simulations, and see some of the compensatory mechanisms at work, by looking at plan-view maps. We again show just the two-ridge case and describe features from a Northern Hemisphere perspective. The left-hand panels of Fig. 4 show maps of the vertically integrated local anomalies of SE and TE AHT. These values are calculated identically to the zonal-mean values, except zonal-integration is not performed, and are referred to as local AHT. The cause of the double-peaked zonal-mean SE AHT structure is clearest in GRaM (Fig. 4a), where poleward local SE AHT is evident at the four corners of each mountain, with the smallest local SE AHT anomaly in the northwest quadrant. This four-corner pattern is caused by the westerly flow splitting ahead of the mountains and causing anomalous northerly flow to advect warmer, moister air, while anomalous southerly flow advects colder, drier air, as was previously described in section 3. Similar features can be discerned in AM2 (Fig. 4d), although the pattern is less defined, and strung out more around a latitude belt. The local TE anomalies are harder to make sense of: there is a tendency for reduced local TE AHT upwind of the ridges and increased local TE AHT in the lee of the ridge (consistent with the inferred storm tracks from Fig. 3), but it is hard to discern the zonal-mean structure, or the differences between models. There is no clear antiphase local relationship between SE and TE AHT changes suggesting that compensation between the two AHT components occurs nonlocally.

To better understand how nonlocal compensation between SE and TE AHT occurs, we look at plan-view plots of near-surface MSE gradient anomalies and local TE AHT anomalies (Figs. 4b,e). Changes to near-surface MSE gradients are created by zonally anomalous meridional winds (associated with the SEs) advecting the mean-state temperatures (Figs. 3b,f,d,h). In GRAM the picture is particularly clear. In the lee of each ridge, there is a region of stronger MSE gradients, caused by circulations connected to SEs to the north and south advecting cold and warm air, respectively, which enhances the MSE gradient between these regions (colors, Figs. 4b,e). Local TE AHT is enhanced in this region due to the increased MSE gradient. However, in the zonal mean, MSE gradients are weakened at latitudes centered on 25° and 55°N; and associated with this is a reduction in zonal mean TE AHT. In general this shows how SEs can influence the MSE gradient that is important for TE AHT. This alteration is one mechanism for how nonlocal compensation between TE and SE AHT can occur. This picture is more difficult to discern in AM2, in part because the MMC is also an important piece of the compensation. This idea of connections between zonal mean TE AHT and zonal mean MSE gradients is explored further in section 3c. We note that changes in local TE AHT are better explained by local MSE gradient changes than by local eddy kinetic energy changes (not shown).

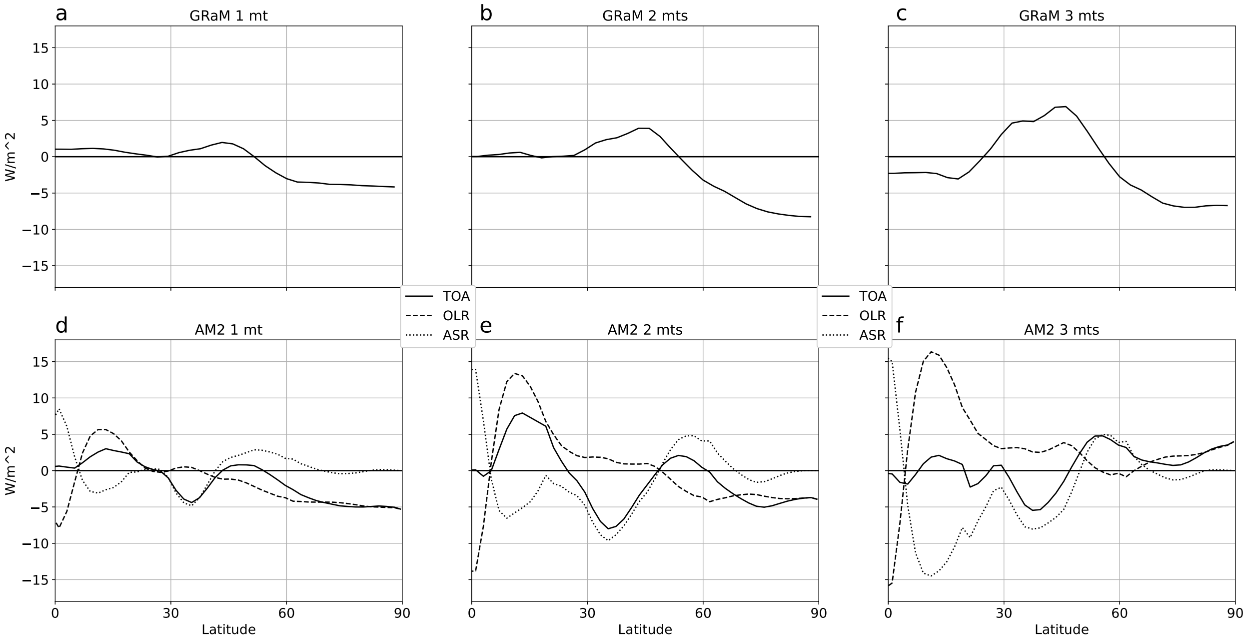

FIG. 5. Anomalies in zonally averaged net TOA radiation, ASR, and OLR for (a)–(c) GRaM and (d)–(f) AM2, where anomalies are calculated as mountain simulation minus control. Upward radiation is defined as negative and downward is defined as positive. Results shown are the mean of the Northern and Southern Hemispheres, which are symmetric by design.

We further investigated compensation between the MMC AHT and eddy AHT in both the Hadley and Ferrel cells. Eddy AHT convergence in the midlatitudes is proportional to the strength of both the mass and heat transport of the Ferrel cell (not shown). Eddy momentum fluxes in the tropics and subtropics scale with the strength of both the mass and heat transport of the Hadley cell (not shown). The Hadley cell undergoes larger changes in AM2 than in GRaM (dots in Fig. 2d versus Fig. 2c), and the eddy momentum fluxes also weaken more in AM2. Changes in the Hadley cell are also influenced by the climatology of the two models, as AM2 has a particularly narrow region of tropical convection, while GRaM has a broader area of tropical convection. Both the connections between eddies and the Ferrel cell and eddies and the Hadley cell are compensatory with stronger eddies reducing the poleward AHT of the MMC.

The local details of plan-view plots and the magnitude of SE AHT differ between simulations and models, but the general principle of AHT compensation and total AHT invariance is found throughout. The dynamic perspective is useful for understanding how atmospheric circulation changes affect AHT, and provides intuition for how these circulation changes give rise to compensation between different AHT components. However, the dynamic perspective does not provide much insight into the degree of compensation. In the next section, we turn to the energetic perspective to provide a more quantitative understanding of why AHT is so nearly invariant.

b. *Energetic perspective on AHT response to orography*

An alternative way to think about AHT is through the energetic requirements implied by the TOA zonal-mean radiation budget. The differences between incoming and outgoing radiation must be balanced by meridional AHT as there is no ocean heat transport (and thus no net surface heat flux) in our model setups. Figure 5 shows the zonal-mean anomalies in TOA radiation caused by the orography for the one-, two-, and three-ridge cases, and for both models. We define downward radiation as positive, and upward radiation as negative, so the climatological ASR is positive and OLR is negative. It is important to note that AHT can alter temperature and cloud-cover patterns, which in turn can alter net TOA radiation. Therefore, ASR and OLR changes do not unidirectionally cause AHT changes, but they do provide useful information to help understand why total AHT is invariant in our simulations.

In GRaM, ASR is constant by construction, so only changes in OLR can contribute to changes in net TOA radiation. Moreover, due to the gray-radiation scheme, changes in OLR arise only from surface and atmospheric-temperature anomalies. As the number of ridges increases in GRaM, the pattern of net TOA radiation anomalies remains similar, but the amplitude increases (Fig. 5, top panels). Within the tropics, anomalies in net TOA radiation are generally less than 3 W m^{-2}. These anomalies are small compared to the overall climatological surplus of net TOA radiation (ASR minus OLR) within the tropics of 41 W m^{-2} in GRaM, and so the anomalies in maximum poleward AHT (i.e., the integral of the tropical net TOA radiation anomalies) are also small. From this perspective, introducing the orography in GRaM has not changed tropical temperatures enough to substantially affect tropical OLR. Therefore, while orography can cause a repartitioning of AHT among its dynamic components, total

AHT must be nearly invariant. In the mid- and high latitudes, changes of OLR in GRaM are consistent with the zonal-mean cooling in the latitude band where the ridges lie and the zonal-mean warming poleward of them (Fig. 3d). Again, the mid- and high-latitude radiation changes are small compared to the climatological deficit of net TOA radiation outside the tropics of -65 W m^{-2} in GRaM, so total AHT is relatively invariant.

The inclusion of clouds in AM2 means that both OLR and ASR can and do change by large amounts (Figs. 5d–f). Changes in zonal-mean net TOA radiation anomalies approach 10 W m^{-2} in the two-ridge case (with even larger values seen in the three-ridge case). However, there is a strong spatial variability, with generally small net TOA radiation changes in the tropics as a whole (tropical-average values range from 0.1 W m^{-2} in the three-ridge case to 3.1 W m^{-2} in the two-ridge case). Therefore, like the results for GRaM, these changes are small compared to the climatological tropical surplus of net TOA radiation of 39 W m^{-2} in AM2, and so changes in AHT are also correspondingly small. In the mid- and high latitudes, mean changes for both ASR and OLR in AM2 are also small compared to the climatological differences in ASR and OLR (the climatological deficit of net TOA radiation outside of the tropics is -68 W m^{-2} in AM2). There is more variation in the latitudinal structure of radiation anomalies in AM2 than in GRaM, likely due to the sensitivity of cloud changes to temperatures and the complex patterns of interference between the responses to individual ridges.

To further explore changes of both ASR and OLR in AM2 we consider plan-view maps for the two-ridge case (Figs. 4c,f). OLR decreases over each ridge due to decreased surface-temperatures associated with the increased elevation of the ridges (Fig. 3h, colors). Away from each ridge, OLR changes (Fig. 4c, colors) are caused by high-cloud changes (Fig. 4c, contours). OLR decreases, and high clouds increase, in both the enhanced storm track downstream of each ridge, and equatorward of each ridge due to changes in precipitation and convection patterns. OLR increases to the southwest of each ridge due to subsidence, and on the equator in regions between each ridge due to shifts in locations of deep convection. In general, the changes to high clouds and OLR also mirror the changes in precipitation patterns (Fig. 3g). ASR patterns are well-explained by changes to total clouds, with ASR decreasing in the previously mentioned areas of precipitation and deep convection changes, albeit with some additional tropical changes due to low cloud changes.

Changes to ASR and OLR in AM2 do not happen in isolation from each other, and compensation between the two helps keep TOA radiation anomalies small. ASR and OLR compensate particularly well near the equator where anomalies in ASR and OLR reach 15 W m^{-2}, but net TOA radiation anomalies are under 1 W m^{-2} [similar to that found in previous observational work of Kiehl (1994)]. Similar compensation, where the anomalies in ASR or OLR are larger than the anomalies in net TOA radiation, can also be seen at other latitudes. However, this zonal-mean compensation does not occur locally in most regions (i.e., ASR and OLR anomalies are not typically collocated). The lack of local ASR and OLR compensation suggests that zonal circulations, such as the Walker cell, are important for limiting zonal-mean net TOA radiation changes. The exception, where weak local compensation does occur, is in the region of enhanced storm activity downstream of each ridge, and equatorward of each ridge. A detailed exploration of the ways in which zonal-mean compensation between ASR and OLR occur, despite the lack of local compensation, is beyond the scope of this work, but could provide interesting avenues for future study.

The detailed patterns of ASR and OLR anomalies that emerge in AM2 are likely not universal. If these same experiments were repeated with different models, some parts of the patterns of radiative anomalies would likely change due to both different cloud responses and different parameterizations of cloud albedo. Even within AM2, the structure of the zonal-mean ASR and OLR changes differs depending on the number of ridges. However, the general principle of ASR and OLR compensation, and relative invariance of net TOA radiation, is more robust. Given these simulations and those of the LGM using comprehensive GCMs (Donohoe et al. 2020), it seems difficult to substantially alter zonal-mean ASR or OLR without altering both of them in compensatory ways, implying that total AHT is relatively invariant in response to orography.

Throughout all of these simulations there are only small changes in net TOA radiation, either because OLR changes are small (as in GRaM) and/or because ASR and OLR compensate each other (as in AM2). One possible reason why the changes in net TOA radiation are small in our simulations and past climates is that the atmosphere is efficient at smoothing temperature anomalies, causing zonal-mean radiation fields to exhibit small overall changes. This idea of smoothing anomalies can be explored through a diffusive perspective on AHT.

c. *Diffusive perspective on AHT response to orography*

From the diffusive perspective, AHT can be characterized as downgradient diffusion of MSE from the equator toward the poles, whose magnitude is set by both the meridional MSE gradient and the atmospheric diffusivity. This perspective has been shown to be effective at explaining AHT and its changes in a range of climates (Flannery 1984; Hwang et al. 2011; Roe et al. 2015; Bonan et al. 2018; Merlis and Henry 2018; Siler et al. 2018; Armour et al. 2019). In this view, the smoothness of total AHT arises because atmospheric dynamics efficiently smooth out bumps or irregularities in MSE. Both dynamic and energetic perspectives are related to the diffusive perspective through the connection between TE AHT and MSE gradients and the smoothly varying zonally averaged TOA radiation climatologies, respectively.

We apply this downgradient transport principle to see how well a diffusive approximation can recreate the AHT response of the GCMs. We use the same moist energy balance model (MEBM) as in previous work (Roe et al. 2015; Liu et al. 2017; Siler et al. 2018; Bonan et al. 2018; Armour et al. 2019), and then make several alterations that are outlined below. In general, the MEBM allows us to test how well both the TE AHT response and total AHT invariance can be explained through downgradient diffusion. We perform an MEBM simulation for each of our mountainous simulations, three for GRaM and three for AM2. In each MEBM simulation we apply a "forcing," $R_f(x)$, that is equal to the divergence of SE and MMC AHT anomalies in response to mountains, as derived from each GCM simulation. In the MEBM, this forcing must be balanced by the combination of radiative feedbacks and downgradient heat transport by TEs, with the balance between these two pieces determining how well the MEBM can compensate for the forcing anomalies and recreate the TE AHT response from the GCM. Mathematically this looks like

$$\lambda T_s'(x) + R_f(x) + = -\frac{p_s}{ga^2} D \frac{d}{dx}\left[(1-x^2)\frac{dh'}{dx}\right], \tag{4}$$

where x is the sine of latitude, λ is the radiative feedback, T_s' is near-surface temperature anomaly, R_f is the forcing, p_s is the surface pressure, g is the acceleration due to gravity, a is the radius of Earth, and D is the climatological diffusivity. The term h' is the near-surface MSE anomaly defined as

$$h'(x) = c_p T_s'(x) + L_v q_s'(x), \tag{5}$$

where c_p is the specific heat of air, L_v is the latent heat of vaporization, and q_s' is the near-surface specific humidity anomaly. The near-surface relative-humidity is assumed to be constant at 80%, so h' is a function of only T_s' and p_s/g is approximated at 10^4 kg m^{-2}. We set $\lambda = -1$ W m^{-2} K^{-1} everywhere. We tested values for λ ranging from 0 to -2.5 W m^{-2} K^{-1} and found that the specific value of feedback has some quantitative effects on the results, but that the general conclusions from this diffusive perspective are not dependent on the specific value chosen for λ. We diagnose values of the diffusivity for both GRaM and AM2 from their control GCM simulation, taking the same approach as Liu et al. (2017). We then spatially average the diffusivity values and use that single value in each of the respective MEBM simulations (1.3×10^6 m^2 s^{-1} for all GRaM simulations and 1.1×10^6 m^2 s^{-1} for all AM2 simulations).

First, the MEBM solves for the T_s' needed to balance the imposed "forcing" subject to linear feedbacks and MSE diffusion. The MEBM's prediction of the TE AHT anomaly (TE′) can then be calculated by integrating the left-hand side of Eq. (4):

$$\mathrm{TE}' = 2\pi a^2 \int_{-1}^{x} [\lambda T's(\hat{x}) + R_f(\hat{x})] d\hat{x}. \tag{6}$$

Note that this formulation does not account for the fact that changes in TE AHT will affect other dynamic AHT components in our climate system (section 3a). However, these calculations are a first-order approximation of how well downgradient diffusion explains the TE AHT response and total AHT invariance in our GCM simulations. The total AHT anomaly in each MEBM simulation is the SE and MMC AHT anomalies that were used to force the MEBM, combined with the calculated MEBM TE AHT anomaly, TE′.

TABLE 1. The absolute value of the ratio of the TE AHT anomaly to the sum of the SE and MMC AHT anomalies for the two-mountain simulations. Results from the GCMs and MEBM are averaged from 20° to 60°.

	Dry theory	GCM ratio	MEBM ratio
AM2	0.77	0.72	0.72
GRaM	0.86	0.93	0.77

The design of these MEBM simulations guarantees that some degree of compensation will occur, as the diffusive, downgradient nature of the MEBM will at least partially compensate the imposed forcing. The degree of compensation can be thought of as a ratio, where the numerator is the response of the system, in this case the absolute value of the TE AHT anomaly, and the denominator is the forcing on the system, in this case the absolute value of the sum of the anomalous SE and MMC AHT. A ratio of 1 would mean perfect compensation and no change in total AHT. A ratio of 0, would indicate no response by the TE AHT to the forcing and would require the forcing to be entirely balanced by the radiative response. Some intuition about the degree of compensation expected can be gained from the analytic solutions to a dry EBM, following, e.g., Held (1999). For a dry EBM, dh/dx in Eq. (4) is replaced with dT/dx, and a new D, D_{dry}, is chosen to match climatology. We calculate D_{dry} identically to how we calculate D, but use near-surface temperature and sensible AHT rather than near-surface MSE and total AHT, and find values of 4.2×10^6 m^2 s^{-1} for GRaM and 2.3×10^6 m^2 s^{-1} for AM2. Again, following Held (1999), we assume that scale of the forcing is governed by a second-order Legendre polynomial. For such a system, the compensation ratio is

$$\frac{|\mathrm{TE}'|}{\left|\int_{-1}^{x} (R_f)\, d\hat{x}\right|} = \frac{6\widetilde{D_{\mathrm{dry}}}}{-\lambda + 6\widetilde{D_{\mathrm{dry}}}}, \tag{7}$$

where $\widetilde{D_{\mathrm{dry}}} = D_{\mathrm{dry}}[c_p p_s/(a^2 g)]$. The left-hand column in Table 1 shows that this dry theory would predict that a forcing coming from a 1-PW anomaly in SE and MMC AHT would generate a diffusive compensation of -0.86 PW TE AHT anomaly in GRaM and of -0.77 PW in AM2.

Figure 6 shows the comparison of TE AHT anomalies (top panels) and the total AHT anomalies (bottom panels) and Table 1 shows the compensation ratio for both the MEBM and GCMs. The top panels show how well the diffusive MEBM approximates the GCM response of the TE AHT to the orography. A perfectly diffusive response would require dashed and solid lines of the same color overlapping entirely. The bottom panels in Fig. 6 depict the degree of total AHT invariance in the MEBM (dashed lines) and GCMs (solid lines). Exact invariance would be zero AHT anomalies.

In both models, TE AHT changes from the GCM are well approximated with the MEBM. The magnitude of the TE AHT anomalies in the MEBM are less than those in the GCM at almost all latitudes, but total AHT is still relatively invariant in the MEBM. Table 1 shows the expected and

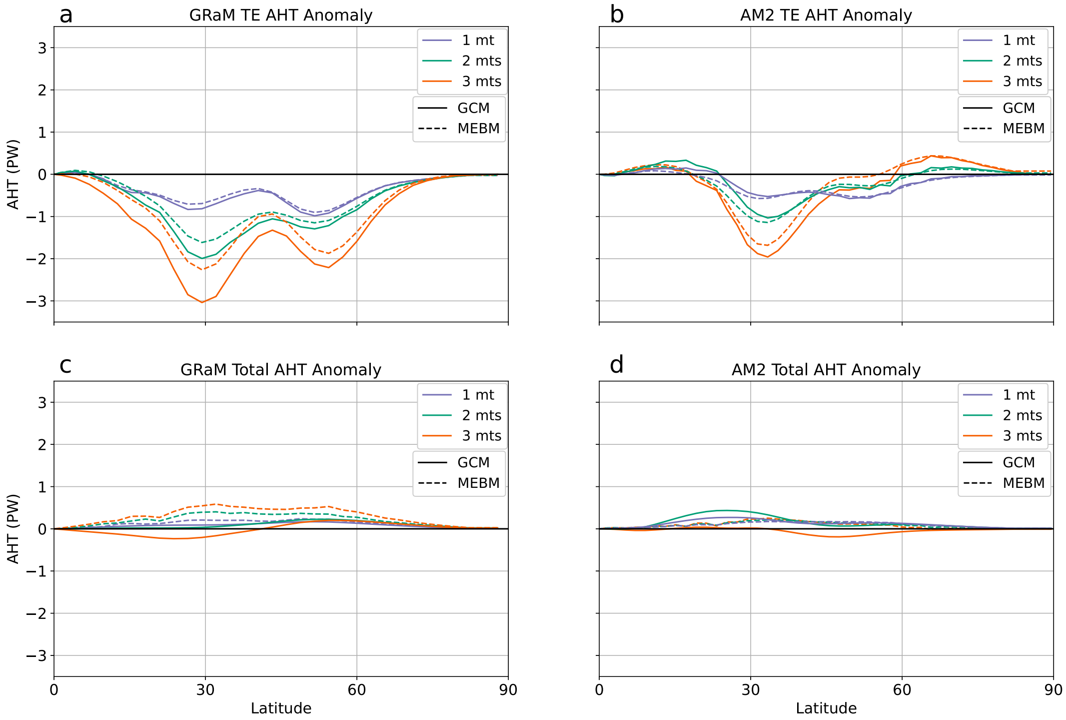

FIG. 6. TE AHT anomalies from the GCM and the MEBM for (a) GRaM and (b) AM2 and total AHT anomalies for the GCM and MEBM for (c) GRaM and (d) AM2, where anomalies are calculated as mountain simulation minus control. Solid lines are for the GCM, and dashed lines are for the MEBM. Results shown are the mean of the Northern and Southern Hemispheres (with the Southern Hemisphere sign flipped), which are symmetric by design.

actual compensation ratios for the two-mountain simulations, with values from the MEBM and GCMs averaged between 20° and 60° latitude. While the actual ratios are in the general range of the theoretical dry ratio, there are discrepancies. These discrepancies likely arise because the GCMs are not operating in a purely diffusive way, and that the GCMs and MEBM include moisture. In GRaM, the compensation is better in the GCM (ratio closer to 1) than in the MEBM, while the AM2 simulation shows similar compensation in both the GCM and MEBM. Despite the differences, both models exhibit compensation ratios close to the ratio from idealized dry theory. As a result, these calculations suggest that the TE part of the response can be understood as a largely diffusive response, and that carries with it a strong tendency toward AHT invariance.

d. *Effect of seasonality on AHT compensation*

We have shown that a high degree of AHT invariance exists even when substantial orography is introduced in two different GCMs. One way to evaluate the robustness of the result is to add a seasonal cycle to our AM2 experiments, which had previously been run at perpetual equinox conditions. Adding seasonality forces the AHT to adjust to both the previously added orography, and also to the large variations in the radiative gradients that drive AHT in the first place.

Seasonality is added by changing the obliquity from 0° to 23.439°. The mixed-layer depth is also increased from 2.4 to 12 m to yield a more Earth-like seasonal cycle of AHT (Donohoe et al. 2014). We only perform seasonal simulations in AM2, as the radiation in GRaM has been tuned to the annual mean. Figure 7 shows the annual-mean AHT and its dynamic components (Fig. 7a) and the AHT anomalies (Fig. 7b); these results should be compared to Figs. 2b,d.

Remarkably, the annual-mean AHT is even more invariant to the addition of mountains when the seasonal cycle is included (solid lines in Fig. 7b versus solid lines in Fig. 2d). Even for the three-ridge case, anomalies in AHT never exceed 0.2 PW, and are mostly less than 0.1 PW. The midlatitudes of the seasonal simulations have similar, but weakened, annual-mean circulation patterns to the perpetual equinox simulations (not shown). The magnitude of the midlatitude AHT anomalies for each of the dynamic components are roughly half that of the perpetual equinox simulations (Fig. 7b versus Fig. 2d). The tropics have larger differences between seasonal and perpetual equinox simulations. In the annual mean, the anomalies in MMC AHT are much smaller in the seasonal simulations than in the perpetual equinox simulations. However, this annual-mean picture obscures substantial monthly anomalies in MMC AHT. Figure 8 shows the anomalous total AHT and its dynamic components for each month for the two-ridge simulation (cf. any given month in Fig. 8 to the annual-mean anomalies in Fig. 7b). In February, there is a nearly 2-PW positive total AHT anomaly just north of the equator in the seasonal two-ridge simulation, when compared to the seasonal control (no orography) simulation. This additional AHT represents a 55% increase in AHT over

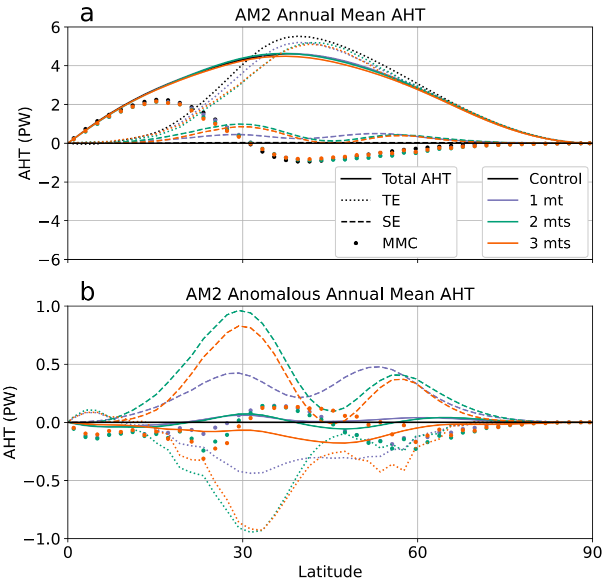

FIG. 7. Total AHT and its dynamic components for (a) the annual mean of AM2 simulations with a seasonal cycle; and (b) the anomalies in annual mean AHT in the AM2 seasonal simulations, where anomalies are calculated as seasonal mountain simulation minus seasonal control. Results shown are the mean of the Northern and Southern Hemispheres (with the Southern Hemisphere sign flipped), which are symmetric by design.

the February control climatology, and comes mostly from anomalous MMC AHT. Then, by June there is little total AHT anomaly near the equator, but come August there is a slightly over 1 PW negative total AHT anomaly. In these seasonal simulations, the tropical response is both time varying and substantially different from the perpetual equinox simulations. Despite these differences, both perpetual equinox and seasonal simulations result in nearly invariant annual-mean total AHT in the tropics. These results suggest that including the seasonal cycle means that invariance is achieved with a different balance of compensating mechanisms, but that the tendency for invariance is, if anything, strengthened.

Within any single month, some degree of compensation can generally be identified among the dynamic components of the AHT, which can be seen where the different dynamic components have different signs in Fig. 8. However, as mentioned earlier, the compensation within any given month is typically much worse than in the annual mean, with monthly AHT anomalies reaching 2 PW, while annual-mean total AHT anomalies are under 0.25 PW (Figs. 7b and 8). Moreover, the combination of compensating dynamic components varies substantially in different months and latitudes. This requires that there is compensation occurring across time, and therefore that seasonal heat storage in the mixed layer is important in compensation between months. At annual time scales, the SE AHT divergence must be balanced by the sum of the radiative response and the TE and MMC AHT changes. However, on monthly time scales with a seasonal cycle, the SE AHT divergence can also be fluxed into the mixed layer. Moreover, since the efficiency of energy exchange between the atmosphere and ocean is almost an order of magnitude greater than the radiative feedback (Barsugli and Battisti 1998), we expect much less AHT compensation on monthly time scales. The heat that is added to, or removed from, the mixed layer during one month is then used in AHT in later months, such that the annual mean shows excellent AHT compensation. When we analyzed the seasonal AM2 output fields, we were unable to draw any general lessons about the specific mechanisms of storage and dynamic compensation. The mechanisms appear complex and regionally variant; and, given the differences between AM2 and GRAM in the annual mean, they may well vary among models.

The strong AHT compensation in AM2 with a seasonal cycle points to the robustness of AHT invariance in response to midlatitude orography. While the mechanisms of this compensation may change between seasons, between models, and between seasonal and perpetual equinox simulations, the compensation in total AHT shows the fundamental flexibility of the atmospheric adjustment.

4. Summary and discussion

Using idealized simulations with midlatitude orography in two general circulation models we find little change in total AHT between our control and mountainous simulations, despite substantial changes in the partitioning of AHT between SEs, TEs, and the MMC. This shows that there is AHT compensation occurring, where changes to the individual dynamic components offset one another. Similar evidence for strong compensation is seen when comparing AHT differences between the Northern and Southern Hemispheres in the modern climate, and when considering simulated AHT changes when LGM ice sheets are imposed. Additionally, total AHT remains smoothly varying, despite substantial latitudinal structure in the changes to individual dynamic components.

The invariance of total AHT is explored through three complementary perspectives. The dynamic perspective (section 3a) shows how changes to circulation and temperature patterns affect dynamic AHT components. Adding midlatitude orography in our simulations creates substantial positive SE AHT anomalies, which are compensated by decreases in both TE and MMC AHT. The compensation between TE AHT and SE AHT dominates in GRaM, while compensation between all three dynamic AHT components plays a role in AM2. This dynamic compensation is similar to that seen between our current climate and the LGM (Donohoe et al. 2020).

The energetic perspective (section 3b) links AHT to the energy required by net TOA radiation. In our simulations without clouds (those using GRaM), the changes in net TOA radiation are entirely due to changes in OLR and are generally small at all latitudes. When a model with a more complex radiation scheme is used (AM2), the changes in net TOA radiation are once again small, even as ASR and OLR changes are larger. This is due to compensations between ASR and OLR as well as large spatial variability that becomes small when taking a spatial average, such that

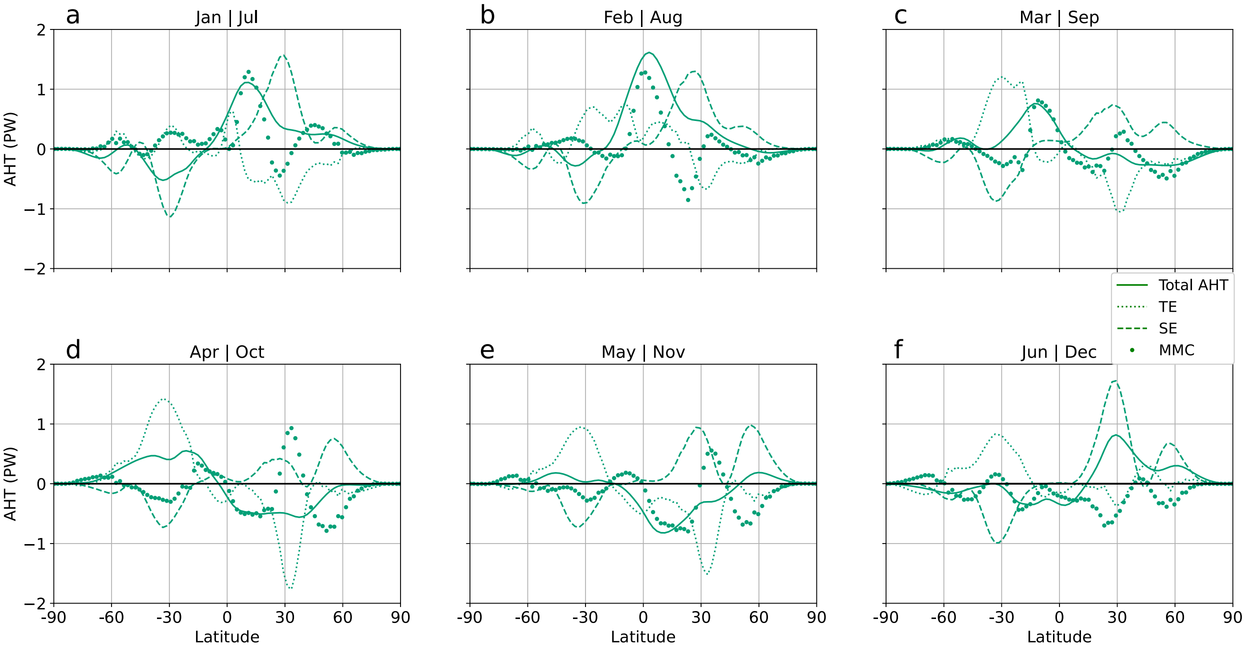

FIG. 8. (a)–(f) Monthly averaged anomalies in total AHT and its dynamic components for the two-mountain AM2 seasonal simulation, where anomalies are calculated as seasonal two-mountain simulation minus seasonal control. The results are symmetric across the equator with a 6-month lag, so to increase the sample size and decrease the number of plots we have combined months by taking months July–December, mirroring them across the equator, flipping the sign, and then averaging them with months January–June. For example, (a) is the AHT anomalies in January and if mirrored across the equator with a sign change, it is also the AHT anomalies for July.

net zonal TOA radiation, and thus AHT, remain relatively invariant.

The diffusive perspective (section 3c) assumes that AHT arises due to the downgradient transport of MSE. When the addition of orography is viewed through this perspective, the question becomes, how well can the atmosphere smooth MSE anomalies created by the addition of the orography? We use a MEBM to explore how well this diffusive perspective can explain the relatively invariant total AHT found in each GCM. We find that our MEBM simulations effectively smooth anomalies such that total AHT remains relatively invariant. The MEBM simulations also show that approximating the TE AHT as a diffusive response works well.

This work does not try to present a comprehensive list of all AHT compensation mechanisms, but instead aims to show the robustness of the principle of AHT compensation in a variety of idealized modeling setups. The addition of seasonality in our simulations provides a sensitivity test for the principle of AHT compensation in response to midlatitude orography. The AHT compensation in the annual mean of seasonal simulations is better than that in perpetual equinox simulations, showing the impressive compensatory ability of the atmosphere.

On Earth, SEs are forced not only by orography, but also by land–sea contrasts and ocean heat transport. Work by Kaspi and Schneider (2013) suggest that total AHT may be less invariant if SEs are forced by zonal anomalies in surface heating. While additional simulations that force SEs in a different manner are beyond the scope of this work, they would present an additional manner of testing the flexibility of Earth's AHT system.

Overall, this work points to Earth's AHT system as being robust and capable of compensating for changes in orography, such that total AHT is relatively invariant. Recent work that used a more complex GCM and probed a variety of SE magnitudes also found little change in total AHT (White et al. 2021). The robust degree of compensation seen in observations; in realistic simulations of the present and past; and in our idealized multimodel numerical experiments in this study, points to the possibility of an underlying dynamic or thermodynamic principle governing this behavior.

Acknowledgments. We acknowledge support for TC, KCA, AD, and GHR from National Science Foundation Award CLD2019647.

Data availability statement. The model data for this study are stored on University of Washington servers and can be made available upon reasonable request to the authors.

REFERENCES

Anderson, J. L., and Coauthors, 2004: The new GFDL global atmosphere and land model AM2–LM2: Evaluation with prescribed SST simulations. *J. Climate*, **17**, 4641–4673, https://doi.org/10.1175/JCLI-3223.1.

Armour, K. C., N. Siler, A. Donohoe, and G. H. Roe, 2019: Meridional atmospheric heat transport constrained by energetics and mediated by large-scale diffusion. *J. Climate*, **32**, 3655–3680, https://doi.org/10.1175/JCLI-D-18-0563.1.

Baggett, C., and S. Lee, 2017: An identification of the mechanisms that lead to arctic warming during planetary-scale and synoptic-scale wave life cycles. *J. Atmos. Sci.*, **74**, 1859–1877, https://doi.org/10.1175/JAS-D-16-0156.1.

Barsugli, J. J., and D. S. Battisti, 1998: The basic effects of atmosphere–ocean thermal coupling on midlatitude variability. *J. Atmos. Sci.*, **55**, 477–493, https://doi.org/10.1175/1520-0469(1998)055<0477:TBEOAO>2.0.CO;2.

Bonan, D., K. Armour, G. Roe, N. Siler, and N. Feldl, 2018: Sources of uncertainty in the meridional pattern of climate change. *Geophys. Res. Lett.*, **45**, 9131–9140, https://doi.org/10.1029/2018GL079429.

Branstator, G., 1995: Organization of storm track anomalies by recurring low-frequency circulation anomalies. *J. Atmos. Sci.*, **52**, 207–226, https://doi.org/10.1175/1520-0469(1995)052<0207:OOSTAB>2.0.CO;2.

Brayshaw, D. J., B. Hoskins, and M. Blackburn, 2009: The basic ingredients of the North Atlantic storm track. Part I: Land–sea contrast and orography. *J. Atmos. Sci.*, **66**, 2539–2558, https://doi.org/10.1175/2009JAS3078.1.

Broccoli, A. J., and S. Manabe, 1992: The effects of orography on midlatitude Northern Hemisphere dry climates. *J. Climate*, **5**, 1181–1201, https://doi.org/10.1175/1520-0442(1992)005<1181:TEOOOM>2.0.CO;2.

Cash, B. A., P. J. Kushner, and G. K. Vallis, 2005: Zonal asymmetries, teleconnections, and annular patterns in a GCM. *J. Atmos. Sci.*, **62**, 207–219, https://doi.org/10.1175/JAS-3361.1.

Chang, E. K., S. Lee, and K. L. Swanson, 2002: Storm track dynamics. *J. Climate*, **15**, 2163–2183, https://doi.org/10.1175/1520-0442(2002)015<02163:STD>2.0.CO;2.

Cook, K. H., and I. M. Held, 1988: Stationary waves of the ice age climate. *J. Climate*, **1**, 807–819, https://doi.org/10.1175/1520-0442(1988)001<0807:SWOTIA>2.0.CO;2.

Cox, T., K. C. Armour, G. H. Roe, A. Donohoe, and D. M. Frierson, 2021: Radiative and dynamic controls on atmospheric heat transport over different planetary rotation rates. *J. Climate*, **34**, 3543–3554, https://doi.org/10.1175/JCLI-D-20-0533.1.

Dawson, A., 2016: Windspharm: A high-level library for global wind field computations using spherical harmonics. *J. Open Res. Software*, **4**, e31, https://doi.org/10.5334/jors.129.

Donohoe, A., and D. S. Battisti, 2012: What determines meridional heat transport in climate models? *J. Climate*, **25**, 3832–3850, https://doi.org/10.1175/JCLI-D-11-00257.1.

——, D. M. Frierson, and D. S. Battisti, 2014: The effect of ocean mixed layer depth on climate in slab ocean aquaplanet experiments. *Climate Dyn.*, **43**, 1041–1055, https://doi.org/10.1007/s00382-013-1843-4.

——, K. C. Armour, G. H. Roe, D. S. Battisti, and L. Hahn, 2020: The partitioning of meridional heat transport from the Last Glacial Maximum to CO_2 quadrupling in coupled climate models. *J. Climate*, **33**, 4141–4165, https://doi.org/10.1175/JCLI-D-19-0797.1.

Farneti, R., and G. K. Vallis, 2013: Meridional energy transport in the coupled atmosphere–ocean system: Compensation and partitioning. *J. Climate*, **26**, 7151–7166, https://doi.org/10.1175/JCLI-D-12-00133.1.

Flannery, B. P., 1984: Energy balance models incorporating transport of thermal and latent energy. *J. Atmos. Sci.*, **41**, 414–421, https://doi.org/10.1175/1520-0469(1984)041<0414:EBMITO>2.0.CO;2.

Frierson, D. M., 2007: The dynamics of idealized convection schemes and their effect on the zonally averaged tropical circulation. *J. Atmos. Sci.*, **64**, 1959–1976, https://doi.org/10.1175/JAS3935.1.

——, I. M. Held, and P. Zurita-Gotor, 2006: A gray-radiation aquaplanet moist GCM. Part I: Static stability and eddy scale. *J. Atmos. Sci.*, **63**, 2548–2566, https://doi.org/10.1175/JAS3753.1.

Held, I. M., 1999: The macroturbulence of the troposphere. *Tellus*, **51A**, 59–70, https://doi.org/10.3402/tellusa.v51i1.12306.

——, and B. J. Soden, 2006: Robust responses of the hydrological cycle to global warming. *J. Climate*, **19**, 5686–5699, https://doi.org/10.1175/JCLI3990.1.

——, M. Ting, and H. Wang, 2002: Northern winter stationary waves: Theory and modeling. *J. Climate*, **15**, 2125–2144, https://doi.org/10.1175/1520-0442(2002)015<2125:NWSWTA>2.0.CO;2.

Holton, J. R., and G. J. Hakim, 2013: *An Introduction to Dynamic Meteorology*. International Geophysics Series, Vol. 88, Academic Press, 552 pp.

Hoskins, B. J., and D. J. Karoly, 1981: The steady linear response of a spherical atmosphere to thermal and orographic forcing. *J. Atmos. Sci.*, **38**, 1179–1196, https://doi.org/10.1175/1520-0469(1981)038<1179:TSLROA>2.0.CO;2.

——, and P. J. Valdes, 1990: On the existence of storm-tracks. *J. Atmos. Sci.*, **47**, 1854–1864, https://doi.org/10.1175/1520-0469(1990)047<1854:OTEOST>2.0.CO;2.

Hwang, Y.-T., D. M. Frierson, and J. E. Kay, 2011: Coupling between arctic feedbacks and changes in poleward energy transport. *Geophys. Res. Lett.*, **38**, L17704, https://doi.org/10.1029/2011GL048546.

Inatsu, M., H. Mukougawa, and S.-P. Xie, 2002: Stationary eddy response to surface boundary forcing: Idealized GCM experiments. *J. Atmos. Sci.*, **59**, 1898–1915, https://doi.org/10.1175/1520-0469(2002)059<1898:SERTSB>2.0.CO;2.

——, ——, and ——, 2003: Atmospheric response to zonal variations in midlatitude SST: Transient and stationary eddies and their feedback. *J. Climate*, **16**, 3314–3329, https://doi.org/10.1175/1520-0442(2003)016<3314:ARTZVI>2.0.CO;2.

Kaspi, Y., and T. Schneider, 2013: The role of stationary eddies in shaping midlatitude storm tracks. *J. Atmos. Sci.*, **70**, 2596–2613, https://doi.org/10.1175/JAS-D-12-082.1.

Kiehl, J., 1994: On the observed near cancellation between longwave and shortwave cloud forcing in tropical regions. *J. Climate*, **7**, 559–565, https://doi.org/10.1175/1520-0442(1994)007<0559:OTONCB>2.0.CO;2.

Li, C., and D. S. Battisti, 2008: Reduced Atlantic storminess during Last Glacial Maximum: Evidence from a coupled climate model. *J. Climate*, **21**, 3561–3579, https://doi.org/10.1175/2007JCLI2166.1.

Liu, X., D. S. Battisti, and G. H. Roe, 2017: The effect of cloud cover on the meridional heat transport: Lessons from variable rotation experiments. *J. Climate*, **30**, 7465–7479, https://doi.org/10.1175/JCLI-D-16-0745.1.

Manabe, S., and T. B. Terpstra, 1974: The effects of mountains on the general circulation of the atmosphere as identified by numerical experiments. *J. Atmos. Sci.*, **31**, 3–42, https://doi.org/10.1175/1520-0469(1974)031<0003:TEOMOT>2.0.CO;2.

Marshall, J., A. Donohoe, D. Ferreira, and D. McGee, 2014: The ocean's role in setting the mean position of the inter-tropical convergence zone. *Climate Dyn.*, **42**, 1967–1979, https://doi.org/10.1007/s00382-013-1767-z.

Merlis, T. M., and M. Henry, 2018: Simple estimates of polar amplification in moist diffusive energy balance models. *J. Climate*, **31**, 5811–5824, https://doi.org/10.1175/JCLI-D-17-0578.1.

Park, M., and S. Lee, 2019: Relationship between tropical and extratropical diabatic heating and their impact on stationary–transient wave interference. *J. Atmos. Sci.*, **76**, 2617–2633, https://doi.org/10.1175/JAS-D-18-0371.1.

Pierrehumbert, R. T., 2010: *Principles of Planetary Climate.* Cambridge University Press, 652 pp.

Ringler, T. D., and K. H. Cook, 1997: Factors controlling nonlinearity in mechanically forced stationary waves over orography. *J. Atmos. Sci.*, **54**, 2612–2629, https://doi.org/10.1175/1520-0469(1997)054<2612:FCNIMF>2.0.CO;2.

Rodwell, M. J., and B. J. Hoskins, 1996: Monsoons and the dynamics of deserts. *Quart. J. Roy. Meteor. Soc.*, **122**, 1385–1404, https://doi.org/10.1002/qj.49712253408.

——, and ——, 2001: Subtropical anticyclones and summer monsoons. *J. Climate*, **14**, 3192–3211, https://doi.org/10.1175/1520-0442(2001)014<3192:SAASM>2.0.CO;2.

Roe, G. H., N. Feldl, K. C. Armour, Y.-T. Hwang, and D. M. Frierson, 2015: The remote impacts of climate feedbacks on regional climate predictability. *Nat. Geosci.*, **8**, 135–139, https://doi.org/10.1038/ngeo2346.

Salustri, G., and P. H. Stone, 1983: A diagnostic study of the forcing of the Ferrel cell by eddies, with latent heat effects included. *J. Atmos. Sci.*, **40**, 1101–1109, https://doi.org/10.1175/1520-0469(1983)040<1101:ADSOTF>2.0.CO;2.

Sasamori, T., 1978: A parameterization of large-scale heat transport in mid-latitudes. Part II. Stationary waves and the Ferrel cell. *Tellus*, **30**, 300–312, https://doi.org/10.3402/tellusa.v30i4.10344.

Siler, N., G. H. Roe, and K. C. Armour, 2018: Insights into the zonal-mean response of the hydrologic cycle to global warming from a diffusive energy balance model. *J. Climate*, **31**, 7481–7493, https://doi.org/10.1175/JCLI-D-18-0081.1.

Stone, P. H., 1978: Constraints on dynamical transports of energy on a spherical planet. *Dyn. Atmos. Oceans*, **2**, 123–139, https://doi.org/10.1016/0377-0265(78)90006-4.

Takahashi, K., and D. S. Battisti, 2007a: Processes controlling the mean tropical Pacific precipitation pattern. Part I: The Andes and the eastern Pacific ITCZ. *J. Climate*, **20**, 3434–3451, https://doi.org/10.1175/JCLI4198.1.

——, and ——, 2007b: Processes controlling the mean tropical Pacific precipitation pattern. Part II: The SPCZ and the southeast Pacific dry zone. *J. Climate*, **20**, 5696–5706, https://doi.org/10.1175/2007JCLI1656.1.

Trenberth, K. E., and S.-C. Chen, 1988: Planetary waves kinematically forced by Himalayan orography. *J. Atmos. Sci.*, **45**, 2934–2948, https://doi.org/10.1175/1520-0469(1988)045<2934:PWKFBH>2.0.CO;2.

——, and D. P. Stepaniak, 2003: Seamless poleward atmospheric energy transports and implications for the Hadley circulation. *J. Climate*, **16**, 3706–3722, https://doi.org/10.1175/1520-0442(2003)016<3706:SPAETA>2.0.CO;2.

Valdes, P. J., and B. J. Hoskins, 1991: Nonlinear orographically forced planetary waves. *J. Atmos. Sci.*, **48**, 2089–2106, https://doi.org/10.1175/1520-0469(1991)048<2089:NOFPW>2.0.CO;2.

Walker, C. C., and T. Schneider, 2006: Eddy influences on Hadley circulations: Simulations with an idealized GCM. *J. Atmos. Sci.*, **63**, 3333–3350, https://doi.org/10.1175/JAS3821.1.

White, R. H., J. M. Wallace, and D. Battisti, 2021: Revisiting the role of mountains in the Northern Hemisphere winter atmospheric circulation. *J. Atmos. Sci.*, **78**, 2221–2235, https://doi.org/10.1175/JAS-D-20-0300.1.

Wills, R. C., and T. Schneider, 2016: How stationary eddies shape changes in the hydrological cycle: Zonally asymmetric experiments in an idealized GCM. *J. Climate*, **29**, 3161–3179, https://doi.org/10.1175/JCLI-D-15-0781.1.